# PEDOT:Tos electronic and thermoelectric properties: lessons from two polymerization processes

Solène Perrot, Florent Pawula, Stanislav Péchev, Georges Hadziioannou, Guillaume Fleury

## To cite this version:

Solène Perrot, Florent Pawula, Stanislav Péchev, Georges Hadziioannou, Guillaume Fleury. PEDOT:Tos electronic and thermoelectric properties: lessons from two polymerization processes. Journal of Materials Chemistry C, 2021, 9 (23), pp.7417-7425. 10.1039/D1TC00756D . hal-03737492

HAL Id: hal-03737492
https://hal.science/hal-03737492v1

Submitted on 25 Jul 2022

# PEDOT:Tos electronic and thermoelectric properties: lessons from two polymerization processes

Solène Perrot,[1‡] Florent Pawula,[1‡, *], Stanislav Pechev,[2] Georges Hadziioannou,[1, *] and Guillaume Fleury[1, *]

[1]Laboratoire de Chimie des Polymères Organiques (LCPO), CNRS UMR 5629 – Université de Bordeaux – ENSCBP, F-33607, Pessac, FRANCE
[2]Institut de Chimie de la Matière Condensée de Bordeaux (ICMCB), CNRS UMR5026, Université de Bordeaux, 87 Avenue du Dr Albert Schweitzer, 33600 Pessac, FRANCE

‡ These authors contributed equally.

*Corresponding author:
florent.pawula@u-bordeaux.fr, georges.hadziioannou@u-bordeaux.fr, guillaume.fleury@u-bordeaux.fr

## Abstract

In the landscape of π-conjugated polymers, poly(3,4-ethylenedioxythiophene) doped with Iron(III) p-toluenesulfonate (PEDOT:Tos) has shown promise as thermoelectric material for near room temperature applications. Such properties are inherent to its semi-metallic nature when optimally doped leading to high electrical conductivity and relatively good Seebeck coefficient. Nevertheless, the final thermoelectric properties of PEDOT:Tos are highly influenced by the polymerization pathways and a thorough understanding of the interplay between polymerization processes and thermoelectric properties is needed. Here PEDOT:Tos thin films with a doping level of 22 ± 2 % were produced by in-situ polymerization and vapor-phase polymerization and a comparative study was performed in order to investigate the subtle correlations between morphological features and electronic signatures for both types of samples. Accordingly, optimized in-situ polymerized PEDOT:Tos films were demonstrated to exhibit higher electrical conductivities (up to 4398 ± 68 $S.cm^{-1}$) and power factors (up to 148 ± 37 $\mu W.m^{-1}.K^{-2}$), highlighting the importance of the polymerization process on the final thermoelectric properties.

## 1. Introduction

For more than twenty years, poly(3,4-ethylenedioxythiophene) (PEDOT), especially in the form of poly(3,4-ethylenedioxythiophene):poly(styrene sulfonate) (PEDOT:PSS) dispersions, is the focus of intense work in the field of organic electronics due to its exceptional electronic properties [1,2]. Alternatively, PEDOT chains can also be doped with other relatively small counter ions like $FeCl_3$, $PF_6$, etc. Among those, the PEDOT doped using iron(III) p-toluenesulfonate (PEDOT:Tos) is highly interesting, inherently to a high electrical conductivity as regards to other organic $\pi$-conjugated materials. In particular, fruitful efforts to balance the antagonistic behavior between the Seebeck coefficient and the electrical conductivity have shed light on PEDOT:Tos as a promising material for thermoelectric applications as a fine tuning of the doping level could lead to high power factor [3]. In-situ polymerization (ISP) and vapor-phase polymerization (VPP) are the two prevailing pathways to polymerize PEDOT:Tos in the form of thin films and extended work has been pursued on the improvement of the Seebeck coefficient and the electrical conductivity by tuning either the oxidation level or crystallinity by synthetic manipulations [3,4]. As a result, PEDOT:Tos is one of the most studied material in the field of organic thermoelectricity. Thermoelectric phenomena are characterized by the conversion of a temperature gradient into an electric potential gradient and vice versa, known as Seebeck and Peltier effects, respectively. Thermoelectric materials can harvest waste heat in useful electrical energy and their efficiency is defined by the dimensionless figure of merit $ZT = \frac{\sigma S^2}{\kappa} T$ with $\sigma$ the electrical conductivity, $S$ the Seebeck coefficient and $\kappa$ the thermal conductivity. Generally, as the thermal conductivity is low for organic materials ($< 1$ W.m$^{-1}$.K$^{-1}$) and not straightforward to measure in a thin film configuration, only the electronic transport properties are investigated and so the efficiency is evaluated through the power factor $PF = S^2\sigma$. The transport properties, i.e. the Seebeck coefficient and the electrical conductivity, are directly related to the density of electronic states (DOS). The DOS defines the number of electronic states that are available in a system per unit volume and energy intervals. The Seebeck coefficient is related to the entropy per charge carrier and is characterized by the measure of an electrical potential difference under a temperature gradient in open-circuit condition [5]. In the classical one band metal model, i.e. in the Sommerfeld free electron gas approximation with a Fermi-Dirac distribution, considering the charge carrier diffusion contribution, the Seebeck coefficient is expressed by the Mott's formula [6]:

$$S(\varepsilon, T) = \frac{\pi^2}{3} \cdot \frac{{k_B}^2 T}{e} \cdot \left( \frac{\partial \ln(\sigma(\varepsilon))}{\partial \varepsilon} \right)_{\varepsilon=\varepsilon_F}$$

With $k_B$ the Boltzmann constant, $T$ the temperature, $e$ the elementary charge and $\sigma(\varepsilon)$ the energy-dependent electrical conductivity.

When $\varepsilon \rightarrow \varepsilon_F$, the energy-dependent conductivity is expressed as $\sigma(\varepsilon) = eN(\varepsilon)\mu(\varepsilon)$ with $e$ the elementary charge, $N(\varepsilon)$ the energy-dependent density of electronic states (DOS) and $\mu(\varepsilon)$ the energy-dependent charge carrier mobility [7]. Therefore, by inserting the energy-dependent electrical conductivity term in the Seebeck coefficient expression, one can notice that $S(\varepsilon, T)$ is function of the density of states $N(\varepsilon)$ and of the charge carrier mobility $\mu(\varepsilon)$, the last term of $S$ becoming $\left( \frac{1}{N(\varepsilon)} \frac{\partial N(\varepsilon)}{\partial \varepsilon} + \frac{1}{\mu(\varepsilon)} \frac{\partial \mu(\varepsilon)}{\partial \varepsilon} \right)_{\varepsilon=\varepsilon_F}$. It is noteworthy that $\frac{\partial N(\varepsilon)}{\partial \varepsilon}$ is the slope of the DOS at $\varepsilon_F$ and is related to the charge carrier density, $n$, through $n = \int N(\varepsilon) f(\varepsilon) d\varepsilon$, with $f(\varepsilon)$ the Fermi-Dirac distribution function [8]. That being said, those parameters do not influence the Seebeck coefficient with the same magnitude. As evidenced previously in PEDOT:Tos thin films [9], $S$ is only slightly dependent on the charge carrier mobility with $S$ approximately proportional to $\mu^{0.2}$ whereas $S$ is well known to strongly depend on the charge carrier density [10,11].

Synthetic manipulations of the ISP process with the addition of various additives (such as pyridine, block copolymer, imidazole…) produced PEDOT:Tos films with conductivity higher than 1000 S.cm$^{-1}$ [9]. Nevertheless, ISP affords a limited control over the polymerization parameters as monomer and oxidant solutions are mixed together, prior to spin coating, leading to a fast polymerization process. On another hand, VPP allows to finely tune the polymerization conditions, i.e. oxidant or additives [12–14], temperature [15,16], pressure and environment [17], time [16,18]; which subsequently leads to an enhanced versatility as regards to the modulation of the electronic properties. By optimizing the VPP synthetic parameters, PEDOT:Tos films with electrical conductivity up to 3305 S.cm$^{-1}$ have been reported, greatly exceeding the electrical conductivity obtained for ISP PEDOT:Tos films [17,19–21]. In particular, Madl *et al.* showed that VPP yields to thinner and smoother films than ISP with higher electrical conductivity, 575 S.cm$^{-1}$ against a maximum of 126 S.cm$^{-1}$, respectively [22]. They explained these differences by the fact that VPP leads to a better packing of the polymer chains because of a slower polymerization process. It is noteworthy that the authors did not use additives in their oxidant solution formulation which could explain the low absolute value of the probed electrical conductivities.

The electronic properties of PEDOT being highly dependent of its semicrystalline nature, several studies examined their interplay by deciphering crystalline modifications upon variations of synthetic pathways. Undoped PEDOT chains crystallize in a monoclinic unit cell in the space group P2/*c* with lattice parameters $a$ = 12.978 Å, $b$ = 7.935 Å, $c$ = 7.6 Å, and $\beta$ = 125.85° while PEDOT doped with tosylate counter-ions crystallizes in an orthorhombic cell in the space group Pmn2$_1$ [23]. Besides, the paracrystalline nature of PEDOT:Tos greatly impact the electronic properties since cumulative disorder inhibits long-range order in contrast to fully crystalline materials. Additionally, the crystallites orientation at the mesoscopic scale, inherent to the film deposition process, also influences the transport properties [24]. By modelling the PEDOT:Tos structure, the unit cell has been found to be orthorhombic with $a$ = 14.0 Å, $b$ = 6.8 Å and $c$ = 7.8 Å and contain four monomer units for one tosylate ion [25]. This structure was unveiled by Aasmundtveit with the assumption that PEDOT chains pack into a lamellar structure where the tosylate ions are positioned between the PEDOT layers. The distance between PEDOT layers depends on the size of the incorporated counter-ion. The orientation of tosylate between PEDOT layers has been investigated by Kim *et al.* [23]. They showed that tosylate is rotated by 33° off the chain axis. Later, by calculations, Shi *et al.* demonstrated how the doping degree (none, lightly, heavily) influences the crystallographic structure of PEDOT:Tos [11]. PEDOT doping leads to a decrease of π-π stacking distance from 3.52 Å for undoped PEDOT, to 3.37 Å for lightly and 3.36 Å for heavily doped PEDOT:Tos which can be explained by strong charge transfer interactions between PEDOT and tosylate. Additionally, increasing the oxidation level leads to an increase of tosylate species which will modify the PEDOT structure from benzoid to quinoid configurations. This change affects the rigidity of the chains and further decreases the π-π stacking distance [11].

Here we present an investigation on PEDOT:Tos thin films produced by ISP and VPP in order to decipher the influence of the synthetic pathways on the thermoelectric properties. In particular, an emphasis was placed on the relationships between the crystallographic structures and the electronic signatures obtained by photoelectron spectroscopy with the aim to evidence the influence of the polymerization process.

## 2. Experimental section

### *2.1 Synthesis of PEDOT:Tos thin films*

3,4-Ethylenedioxythiophene (EDOT) solution was purchased from TCI chemical. The oxidant solution, 54 wt.% of Iron(III) p-toluenesulfonate ($Fe(Tos)_3$) in butanol (Heraeus Clevios CB54-V2), was used as a stock solution and modified with addition of butanol to obtain the desired concentration. Pyridine and DMSO was purchased from Acros Organics and Sigma Aldrich, respectively. All chemicals were used as received without further purification. Solutions containing 40 wt.% of tosylate was prepared with addition of 0.5 mol of pyridine for 1 mol of $Fe(Tos)_3$. A high boiling point solvent (DMSO) was added in a volume fraction of 3% with respect to the oxidant solution volume. The solution was stirred for 12h at room temperature and then stored at 4°C. Intrinsic and doped silicon wafers purchased from Sil'tronix were used as substratedepending on the characterization technique. The substrates were cleaned in isopropanol, ethanol and acetone ultrasonic baths during 10 minutes for each step.

ISP was performed by the addition of EDOT monomers to the $Fe(Tos)_3$ oxidant solution containing additives with an oxidant-to-monomer ratio equal to 2.3:1 (i.e. 2 mol of oxidant for the polymerization and 0.3 mol for the doping of the conjugated system). The solution was stirred for 10 s, filtered and then spin-coated on 15x15 mm substrate at 1500 RPM for 30 s. Films were annealed at 100°C for 15 min. Finally, the films were washed with 1-butanol and ethanol in order to remove the excess of oxidant and additive and dried under air flow.

VPP was performed by spin-coating $Fe(Tos)_3$ oxidant solutions (previously filtered with a 0.22 µm PTFE filter) at 1500 RPM for 30 s on a cleaned substrate. The samples were then placed in a vacuum chamber held at 70°C containing a reservoir of EDOT monomers (30 µL) under static vacuum during 5 min in order to initiate the VPP process. After the polymerization, the samples were rinsed in ethanol in order to remove excess of oxidant and additives and dried under air flow.

### *2.2 Characterization methods*

Photoelectron spectroscopy measurements (X-Ray Photoelectrons Spectroscopy (XPS) and Ultraviolet Photoelectrons Spectroscopy (UPS)) were performed in an SPECS ultrahigh vacuum chamber at the ELORPrintTec platform. For UPS, measurements were obtained using He(I) with a low intensity UV light (21.22 eV). XPS measurements were performed using a monochromatized Al Kα X-ray source with an energy of 1486.6 eV. XPS spectra were fitted with the help of CasaXPS software keeping the same constraints for each fitting (peak envelope as Gaussian-Lorentzian (70-30), constant full width at half maximum for all contributions and 2:1 area ratio between $S2p_{1/2}$ and $S2p_{3/2}$ signals). All the PEDOT:Tos films deposited on doped Si substrates were stored in a glove box before being analyzed by photoelectron spectroscopy in order to avoid environmental contaminations.

Grazing Incident X-ray Diffraction (GIXRD) data were recorded at room temperature on a Bruker D8 Discovery diffractometer equipped with a LynxEye detector using Cu Kα radiation in θ-2θ mode with a grazing incident angle of 0.6° and divergence slit of 0.05 mm. Diffraction profiles of PEDOT:Tos films on intrinsic Si substrates were fitted with the help of X'Pert HighScore Plus software (PANalytical B. V.). Regarding the very broad diffraction peak of nanocrystals in amorphous matrix, the small diffractometer contribution to the peak broadening was neglected during the analysis. To decipher the crystallite orientation, the angular dependency of the X-ray intensity was corrected using the Lorentz polarization factor, $\mathrm{LP}(\theta) = \frac{1+\cos^2(2\theta)}{\sin^2(\theta)\cos(\theta)}$. The Lorentz correction factor, $\mathrm{L}(\theta) = \frac{1}{\sin^2(\theta)\cos(\theta)}$, is used to correct the X-ray intensities in order to calculate structure factor values independent on the geometry of data collection, while the polarization factor, $\mathrm{P}(\theta) = \frac{1+\cos^2(2\theta)}{2}$, takes into account the partial polarization of the X-ray beam on reflection by the substrate. Following this procedure, the normalized [020] (face-on) integrated intensity was converted into an equivalent normalized

[100] (edge-on) integrated intensity allowing one to accurately estimate the edge-on fraction (and vice-versa) [24,26]. Table S1 provides the details of the normalization procedure.

Atomic Force Microscope (AFM) using a Dimension FastScan AFM (Bruker) in tapping mode with silicon cantilevers (Fastscan-A, typical tip radius of ≈ 5 nm and resonance frequency of the cantilever of ≈ 1.25 kHz) was used to record the morphological features of films on intrinsic Si substrates with gold contacts 100 nm thick. The root mean square roughness Rq were estimated on 4 $\mu m^2$ surfaces using Gwyddion software. The high resolution current mapping images were recorded simultaneously using Peak Force Tunneling AFM (PF-TUNA, Bruker) under 1 $nA.V^{-1}$ and a DC voltage bias of 2V.

Resistance ($R$) of the film with bottom gold contacts (100 nm thick) on intrinsic Si substrate was measured using 4-point probe apparatus. Sheet resistance ($Rs$) was calculated by multiplying $R$ by a geometric factor of 4.2209 [27] taking into account the square shaped sample and the 15:1.6 ratio between the sample dimension and the probe-to-probe distance. 4-probe measurements were repeated at least 3 times on 3 films for each sample. The film thickness ($t$) was obtained by scratching a film using a Bruker DEKTAK XT-A profilometer. By coupling those two methods, the electrical conductivity of each sample were determined using $\sigma = 1/(Rs \cdot t)$.

The Seebeck coefficient ($S$) measurements were performed on a homemade apparatus in a thin film configuration on samples with bottom gold contacts (100 nm thick) on rectangular intrinsic Si substrates. The temperature gradient was induced with two Peltier plates monitored by temperature controllers via two Teflon-insulated copper/constantan thermocouples (OMEGA) attached to the gold contacts with a droplet of silver conductive paint (RS PRO). Thermal contact between the sample and the Peltier plates was ensured using a high thermal conductivity paste (OMEGATHERM 201). The thermoelectric voltage was measured on the silver conductive paint droplet, with two tungsten pins connected to a nano-voltmeter (Keithley).

Seebeck coefficient was calculated by measuring thermoelectric voltage $\Delta V$ at different temperature gradient and fitting with a straight-line $S = -\Delta V/\Delta T$.

## 3. Results and discussion

PEDOT: Tos films were prepared either by ISP or VPP using an $Fe(Tos)_3$ oxidant solution at 40 wt.% in 1-butanol containing pyridine and DMSO as additives. As shown in **Figure 1 (a, b)**, both polymerization techniques lead to drastically different surface textures. ISP films show a sponge-like structure in which PEDOT:Tos appears to constitute a structure skeleton. Conversely, VPP films are composed of sintered PEDOT:Tos dots. Interestingly ISP films exhibit a lower surface roughness (3.0 and 9.3 nm for ISP and VPP, respectively), inherent to the growth process mechanisms. Indeed, a nucleation and growth process is responsible of the granular structure observed for VPP films; PEDOT:Tos nano-aggregates are continually formed at the top surface of the oxidant layer during the process [21]. This kind of morphology is consistent with previous reports on VPP PEDOT:Tos films [15,28]. The roughness of the film is often associated with the redox activity of the oxidant, here $Fe(Tos)_3$ [29] which is tailored by the presence of pyridine in the formulation. In particular, we speculate that the reduced pressure employed for the VPP process might influence the control of the redox activity of $Fe(Tos)_3$ by pyridine [15]. A higher redox activity in VPP yields to a faster polymerization kinetics concomitant with an increase of the number of nucleation sites at the liquid/vapor interface, leading to rougher films.

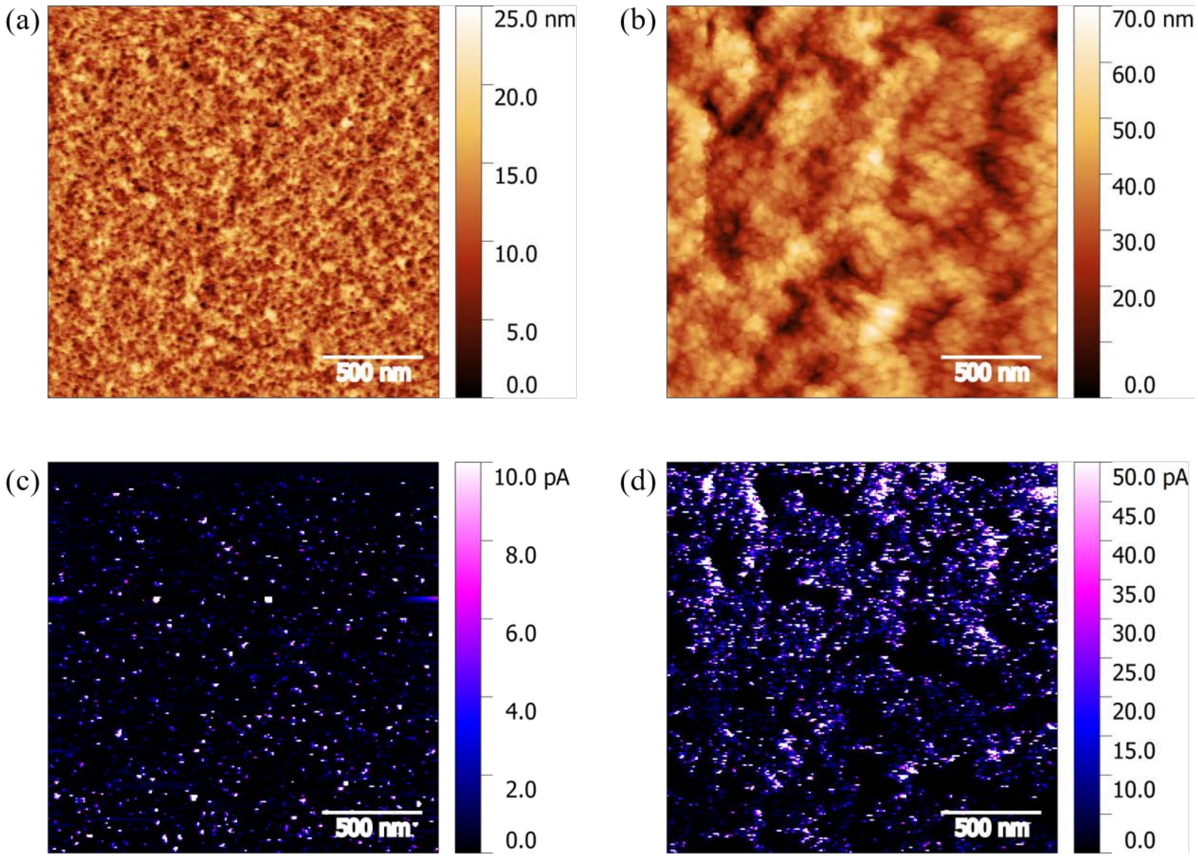

**Figure 1:** 2×2 μm$^2$ topographical and high resolution current mapping AFM images of (a, c) ISP PEDOT:Tos and (b, d) VPP PEDOT:Tos films.

The high resolution current AFM mapping allows us to probe percolated pathways perpendicular to the film surface (in contrast to the 4-probe method used for the measurement of the macroscopic electrical conductivity linked to in-plane charge transport), as shown in **Figure 1 (c, d)**. For ISP films, the current paths distribution is rather homogeneous, in agreement with a continuous sponge-like structure. In contrast the current paths are heterogeneously distributed for VPP films in direct relationships with the surface texture but higher current values were observed for the highly conductive areas. Such inhomogeneity suggests breaks of the percolation paths at the mesoscopic level in the in-plane direction which could have a detrimental effect on the transport properties for VPP films (*vide infra*).

The composition of both ISP and VPP samples was probed by XPS. Oxygen, carbon and sulfur signals appeared on the survey spectrum. These three elements were finely analyzed in order to deduce the composition of the ISP and VPP samples. The fittings are presented in **Figure 2**. O1s fitting shows the contribution of oxygen atoms in PEDOT at 533.51 eV, $PEDOT^+$ at 534.93 eV, and in tosylate at 531.95 eV and 531.01 eV. At 536.49 eV, the π to π* shake up signal corresponding to ejected core electrons which collide with the shared electrons in the π orbital of the ring structure is apparent [30]. The S2p XPS spectra was used to estimate the oxidation level (doping level) of the PEDOT:Tos films as sulfur is a common element of tosylate and PEDOT. Considering the semi-crystalline nature of PEDOT:Tos, Gaussian or Gaussian-Lorentzian (90:10) were used for the fitting process [31]. Both signals at 164.1 and 165.1 eV correspond to the doublet from the thiophene unit of PEDOT. Through doping, delocalized charges are created on the PEDOT structure and the presence of PEDOT cations is visible with the doublet at 165.5 and 166.4 eV. Since some of the tosylate molecules do not participate to the doping, two additional doublets have to be taken into account. One at 167.4 and 168.0 eV, is attributed to the tosylate involved in the doping mechanism [32], and another one at 168.7 and 169.8 eV is attributed to unreacted tosylate which are still present inside the film. This result signifies that an amount of unreacted tosylate molecules is still present inside the film despite the washing steps. The oxidation level was then determined through the ratio between the areas under the peak contributions of tosylate molecules participating to the doping and the total contributions of sulfur atoms [33]. Hence, an oxidation level for both ISP and VPP films equal to 22 ± 2 % was calculated. This result shows that the oxidation of the PEDOT chains is not affected by the polymerization pathways even if drastically different morphological features are obtained at the mesoscopic scale. The maximum theoretical oxidation of PEDOT by tosylate molecules is 33% (which signifies that one tosylate can be found every three monomer units [34], [35]), but this result is consistent with previous studies on PEDOT:Tos produced by ISP or VPP

[32], and is often referred as an optimal value for thermoelectric application due to a favorable balance between the Seebeck coefficient and the electrical conductivity [36].

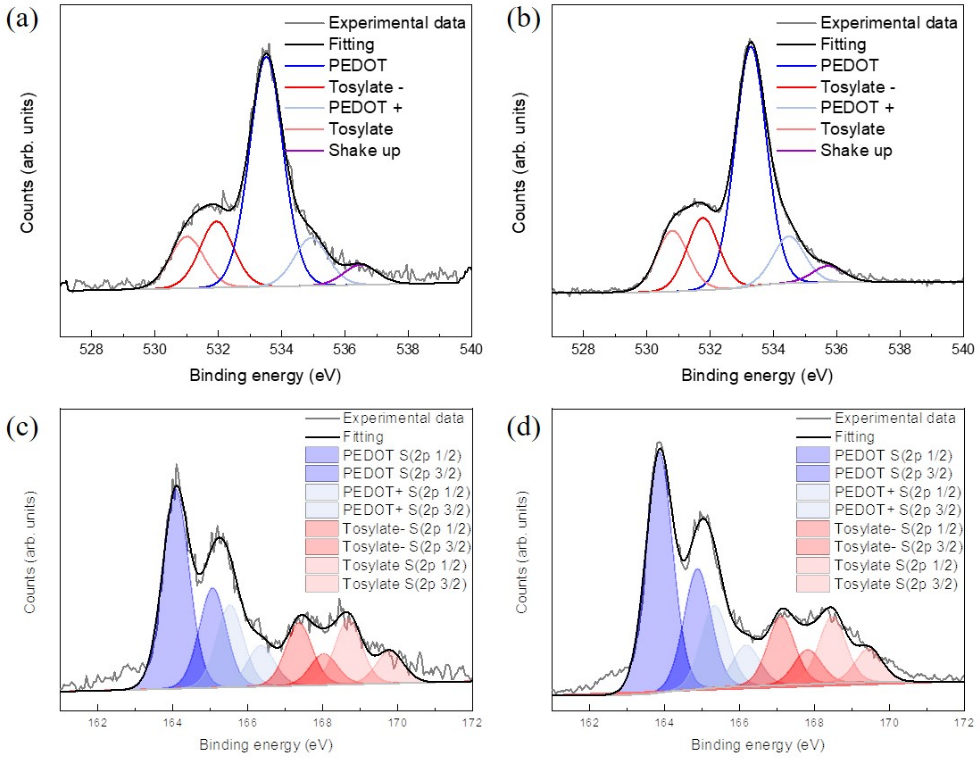

**Figure 2:** XPS fitting of O1s and S2p signals of ISP and VPP films. (a) O1s ISP, (b) O1s VPP, (c) S2p ISP, and (d) S2p VPP. Blue and red areas represent signals linked to S2p in PEDOT and tosylate, respectively.

To better understand the microstructure of PEDOT:Tos chains with respect to the polymerization processes, grazing incidence X-rays diffraction (GIXRD) has been performed. Regarding the paracrystalline nature of PEDOT:Tos, a quantitative analysis of the GIXRD data is hazardous because the broadening of the diffraction peaks does not allow a proper Le Bail refinement. Hence, in order to investigate the influence of the polymerization technique on the crystallographic structure, we present a qualitative sample to sample comparison based on a line profile fit considering a literature-based orthorhombic lattice with *a* ~ 14.2 Å and *b* ~ 7 Å [25]. As ISP and VPP generate PEDOT:Tos films following different growth processes, slightly different crystallographic characteristics were revealed as described in the following. First of all, ISP and VPP diffraction patterns show four broad diffraction peaks, attributed to (100), (200), (300) and (020) Bragg plans, as displayed **Figure 3**. The position and the width of these peaks have been fitted in order to determine the crystallography characteristic values which are reported in **Table 1**.

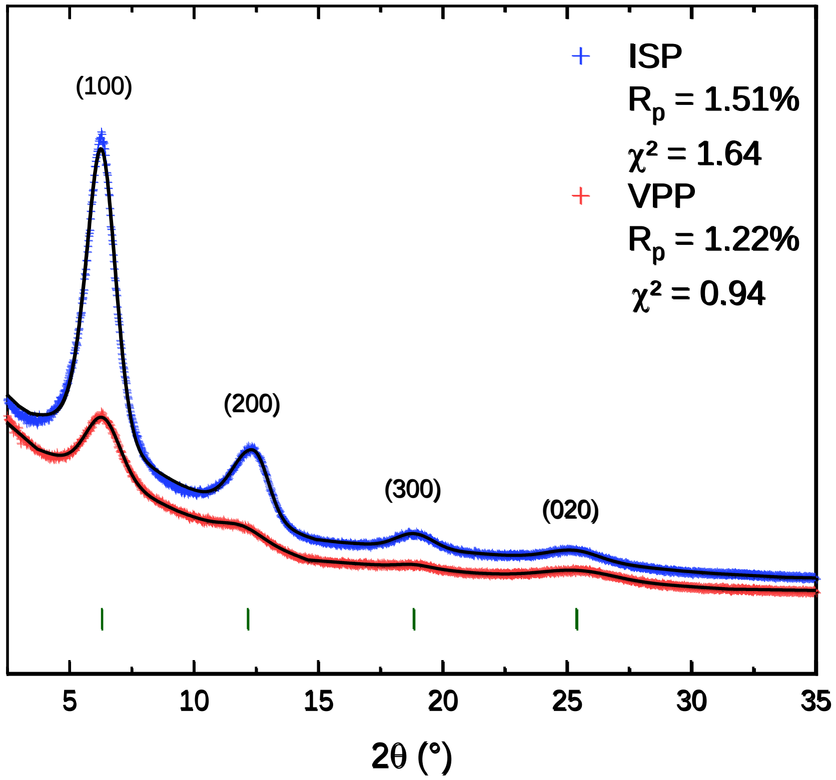

**Figure 3:** GIXRD profile with measured (crosses) and fitted (black line) data along with their agreement indices. Vertical ticks are the Bragg peak positions considering an orthorhombic unit cell with a ~ 14.2 Å and b ~ 7 Å [25].

According to Bragg's law, the diffraction peak position is related to the interplanar distances. Therefore, the lamellae ($d_{lamellae}$) and the π-π ($d_{\pi-\pi}$) stacking distances can be straightforwardly deduced from the *h00* and *020* peaks positions, respectively. As reported in **Table 1**, the $d_{\pi-\pi}$ is smaller for VPP samples with 3.50 ± 0.01 Å and 3.53 ± 0.01 Å for ISP ones. The π-π staking distance is crucial in conjugated polymers and plays a role in the hopping mechanism of charge carriers and this result would suggest a slightly enhanced charge transport along the π-π direction for samples made by VPP. On the other hand, the $d_{lamellae}$ is higher for VPP samples with 14.28 ± 0.02 Å *versus* 14.17 ± 0.04 Å for ISP films, which conversely suggests a better transport for ISP samples along the inter-lamellae direction [37].

**Table 1:** Crystallographic parameters extracted from the profile fit analysis of GIXRD pattern of PEDOT:Tos films made by VPP and ISP, with $d_{lamellae}$ ($d_{\pi-\pi}$) being the lamellae (π-π) stacking distance, $L_c$ being the crystallite size, $L_c/d_{lamellae}$ being the average chain number in a crystallite, rC being the relative crystallinity and Face-on Orientation being the crystallites face-on orientation fraction. Figures between parenthesis denote the standard deviation on three samples.

| | $d_{lamellae}$ (Å) | $d_{\pi-\pi}$ (Å) | $L_c$ (Å) | $L_c/d_{lamellae}$ | rC arb. unit | Face-on Orientation (%) |
|---|---|---|---|---|---|---|
| VPP | 14.28(2) | 3.50(1) | 47.2(8) | 3.31(6) | $0.8(2)\times10^{-3}$ | 51(6) |
| ISP | 14.17(4) | 3.53(1) | 50.1(4) | 3.54(2) | $1.7(3)\times10^{-3}$ | 80(3) |

Secondly, the ISP diffraction peaks are much sharper than the VPP ones suggesting that ISP samples are more crystalline. Meanwhile broader peaks for VPP samples suggest smaller and/or more disordered crystallites. By fitting the *100* peak profile, it is possible to estimate the relative crystallinity, rC, when compared between samples whose diffraction patterns are recorded in the exact same conditions. As can be seen in **Table 1**, the ISP rC is approximately twice higher than the VPP one, confirming that ISP results in a higher crystallinity. This is supported by the coherence length, $L_c$, analysis showing smaller crystallites in VPP samples, 47.2 ± 0.8 Å against 50.1 ± 0.4 Å for ISP samples, taking into account the cumulative disorder, i.e. considering the peaks widening at higher diffraction order [38]. Concomitantly, a smaller average chain number in one crystallite ($L_c/d_{lamellae}$) is observed in VPP films than in ISP films, 3.31 ± 0.06 against 3.54 ± 0.02. This parameter is characteristic of the packing quality of the crystallites in the PEDOT:Tos samples. A higher value hints an improved macroscopic electrical conductivity as recently demonstrated by Dong *et al.* for PEDOT:PSS [39]. To sum up, by comparing the GIXRD patterns of samples made by both techniques, PEDOT:Tos films are more crystalline when they are in-situ polymerized demonstrating a smaller lamellae stacking distance, a slightly higher π-π staking distance, a higher crystallite size together with a higher average chain number and most importantly a twice higher relative crystallinity. Hence, these result suggest a better charge carrier transport in ISP films.

Despite the importance of crystallinity on the charge carrier mobility in polymer films, the orientation of crystallites plays also a key role in the transport mechanism through the hopping between conjugated chains. Petsagkourakis *et al.* demonstrated the influence of additives on the orientation of crystallites for ISP films [4] while Chen *et al.* reported a similar study on VPP films [40]. Both studies were conducted on PEDOT:Tos films deposited on glass substrate and the preferential orientation was found to be edge-on in both cases. At first sight, these results appear in accordance with our data as similar ratios between the [001] and [020] peak intensity hint a constant majority fraction of edge-on crystallites for ISP and VPP films. Nevertheless, one has to consider the angular dependency of the X-ray intensity and the thickness-normalized integrated intensity in order to properly evaluate the fraction of edge-on or face-on crystallites (see the experimental section and Table S1 for further details). Taking into account these requirements through the use of the Lorentz polarization factor, the analysis reveals a face-on orientation highly superior in the ISP films as compared to the VPP films, i.e. 80 ± 3% and 51

± 6% respectively. It is commonly reported in literature that the face-on orientation is preferred in PEDOT films with small counter-ions like $Cl^-$, $Br^-$ and $HSO_4^-$ [41], in contrast to bigger counter-ions like PSS, Tos and OTf leading to an edge-on preferred orientation [24,42]. Nevertheless, polymerization conditions, dopant nature, etc. can drastically change the main crystallite orientation as reported PEDOT:Cl films prepared by oCVD [24]. Besides, the substrate nature has been shown to further direct the orientation of crystallites in PEDOT:Tos films as demonstrated by Franco-Gonzalez [43]. Indeed, PEDOT:Tos crystallites were demonstrated to preferentially orient face-on on ordered substrates (i.e. Si) while an edge-on orientation was observed on amorphous substrates (glass).

Additionally, the inherent disorder nature of PEDOT:Tos strongly influences the charge carriers transport properties as charge transport occurs by phonon-assisted hopping of bipolarons. The doping of PEDOT by tosylate anions leads to the creation of bipolaron states between the valence band and the conduction band, inducing a reduction of the band gap from 1.7 eV [44,45] for a single neutral chain to 0.5 eV for a p-doped PEDOT [46]. For highly doped PEDOT:Tos systems, the aforementioned bipolaronic band overlaps with the valence band inducing semi-metallic behavior. Through doping, the tosylate counter-ions are randomly distributed in the sample, inducing a spatially varying electrostatic potential and so, charge carriers experience heterogeneous binding energies, concomitantly with heterogeneous vacuum levels at the surface ($\varepsilon_{vac}^{s}$). Therefore, as UPS measures the energy difference between $\varepsilon_{vac}^{s}$ and the irradiating energy $h\upsilon$, this technique provides useful information on the spatially varying electrostatic potential, i.e. a disorder character, which is directly related to the randomly distributed tosylate anions along the PEDOT chains. As demonstrated for PEDOT:Tos with a multiscale realistic morphological model [46], the broad range of $\varepsilon_{vac}^{s}$ is at the origin of the observed Gaussian tail broadening of ~ 1 eV in UPS spectra, in contrast to the commonly DOS broadening of ~ 0.1 eV observed with other techniques. Hence, the broad tail is characteristic of a heterogeneous electrostatic potential and so, of the disorder induced by the anions distribution in the sample. UPS spectra for ISP and VPP samples are shown **Figure 4**. In the cut-off region **Figure 4 (a)**, at low kinetic energy, ISP and VPP films have similar work functions of 4.3 eV. As the work function is characteristic of the top surface of the film, these results demonstrate that VPP and ISP PEDOT:Tos provide similar electronic surfaces. However, small differences are observed in the valence band region (1 eV < $\varepsilon_B$ < 6 eV), see **Figure 4 (b)**. Despite the fact that the spectral features of this region are characteristic of the DOS of the tosylate counter-ion and of the monomer unit chemical bonds [47], those small differences can arise from different crystallite orientation, packing density and morphology [48,49]. In this region, when the binding energy tends to 0 eV (see the inset of **Figure 4 (b)**), the curves are similar and reveal the semi-metallic behavior with a small amount of electronic states near the Fermi level [50]. According to the Mott's formula, the slope of the density of states at the Fermi level is proportional to the Seebeck coefficient. As the slope at 0 eV for both sample types are rather similar, this suggests a quasi-equal Seebeck coefficient for both polymerization methods. Nevertheless, the disorder inherent to the randomly distributed tosylate counter-ions should be taken into account as the Gaussian broadening induced by the heterogeneous electrostatic potential can influence the DOS tail broadening. Also, it is noteworthy that the influence of the doping level on the DOS broadening has been calculated and revealed itself to be barely insensitive [46]. Fitting the valence band tail broadening with a Gaussian function enables the qualitative characterization of the disorder character of the counter-ions distribution by comparing the Gaussian width between ISP and VPP samples. As shown in **Figure 4 (c)**, Gaussian fits have been performed in the same energy range, close to the Fermi energy. Analyzing the fits, with quality criteria R > 0.994, leads to full width at half maximum values of 0.54 ± 0.04 eV and 0.51 ± 0.02 eV for ISP and VPP films, respectively, which is almost twice lower than the expected broadening and 5 times higher than the DOS broadening, consistent with the expected DOS hidden signature. Such close values with respect to the uncertainties suggest very similar disorder characters of the $Tos^-$ distribution with a trend to slightly higher disorder in the ISP film. Besides, the HOMO level values of both films are different. The HOMO level of the ISP film is at 1.42 eV compare to 1.25 eV for VPP. The HOMO level is linked to the ionization potential (IP) since IP is the energy needed to ionize the material, i.e. the higher the HOMO level energy, the higher the energy needed to extract an electron from this molecular orbital. This difference is consistent with different crystallites orientation and surface morphologies as evidenced on perylene-derivative and on α,ω-dihexyl-sexithiophene films [48], [49].

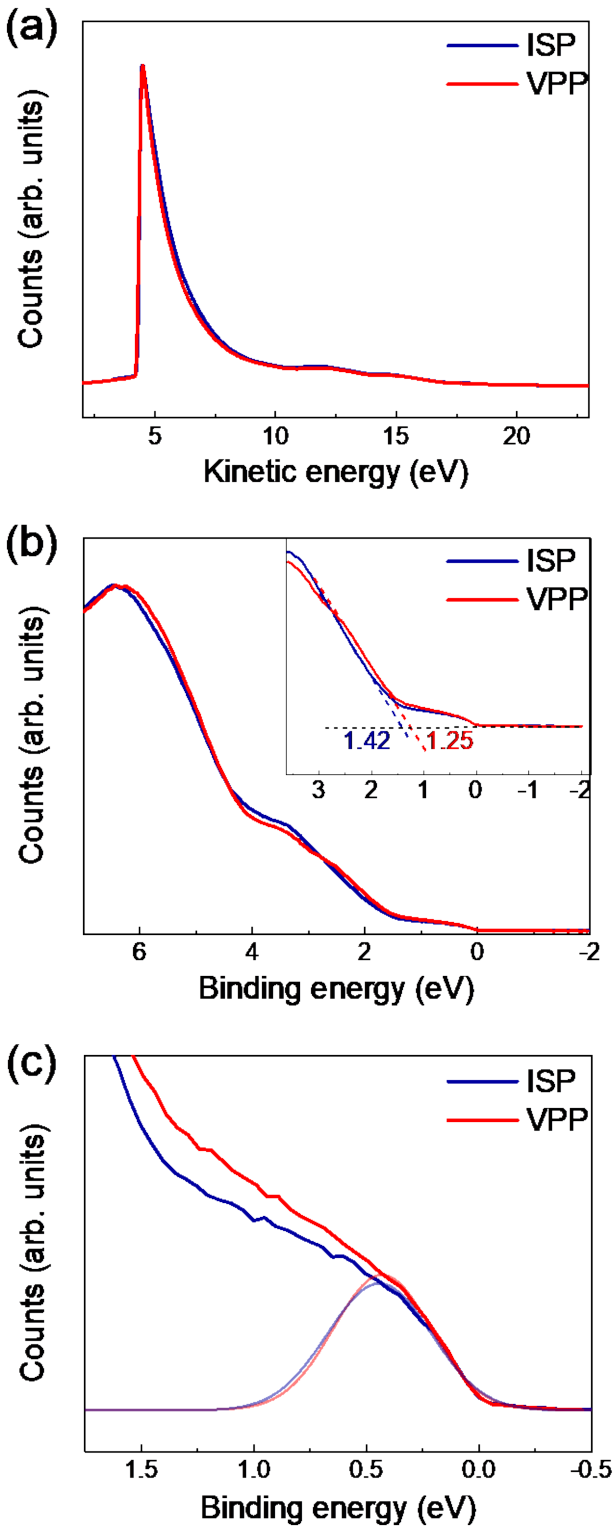

**Figure 4:** UPS spectra of PEDOT:Tos films made by ISP and VPP. (a) Cut-off region showing the work function, (b) Valence band region of the material, and (c) Gaussian fits of the valence band tail.

The electrical conductivity for both polymerization routes is reported in **Figure 5**. The electrical conductivity is approximately 1.5 times higher for ISP films, 4398 ± 68 S.cm$^{-1}$, compared to VPP films, 3025 ± 67 S.cm$^{-1}$. We believe that the structural inhomogeneity observed by high resolution current mapping (see **Figure 2**) is a signature of the lower macroscopic electrical conductivity measured by the 4-probe method for the VPP samples despite the higher recorded current values. Note that, compared to [22], the high conductivity values observed here are most probably due to the advanced chemical formulation and high quality measurements, i.e. the use of additives and gold contacts, respectively. As shown by the XPS spectra analysis, the doping level, is independent of the polymerization process. This suggests similar carrier density in both sample types. Therefore, considering $\sigma = ne\mu$, where $n$ is the carrier density, $e$ the elementary charge and μ the charge carrier mobility, the difference in conductivity values has to be induced by different mobilities. This is consistent with the crystallographic and morphological analysis because the higher the relative crystallinity, the better the charge mobility, the higher the conductivity, as found out for ISP films. This result is also supported by the current mapping analysis where homogeneously distributed percolative pathways has been observed in the case of ISP PEDOT:Tos film, supporting a better conduction at the macroscopic scale.

The Seebeck coefficient of ISP and VPP films has also been measured at room temperature, see **Figure 5**. The measured values are almost the same with 18.4 ± 2 and 18.4 ± 0.7 µV.K$^{-1}$ for ISP and VPP PEDOT:Tos, respectively, which is consistent with a similar charge carrier density. Accordingly, this suggests an insensitivity of the DOS slope at the Fermi level with respect to the polymerization technique. As the Seebeck coefficient is not only dependent on the charge carrier density but also on the carrier mobility, this result might be surprising. However, it has been demonstrated previously the very weak influence of the charge carrier mobility on the Seebeck coefficient [9]. Therefore, as the electrical conductivity is higher for ISP samples, the power factor (PF) is higher for the ISP PEDOT:Tos than for the VPP one, 148 ±

37 µW.m$^{-1}$.K$^{-2}$ and 103 ± 11 µW.m$^{-1}$.K$^{-2}$ respectively. From a thermoelectric point of view, this result demonstrates that ISP films are more prone for integration in thermoelectric devices than VPP ones.

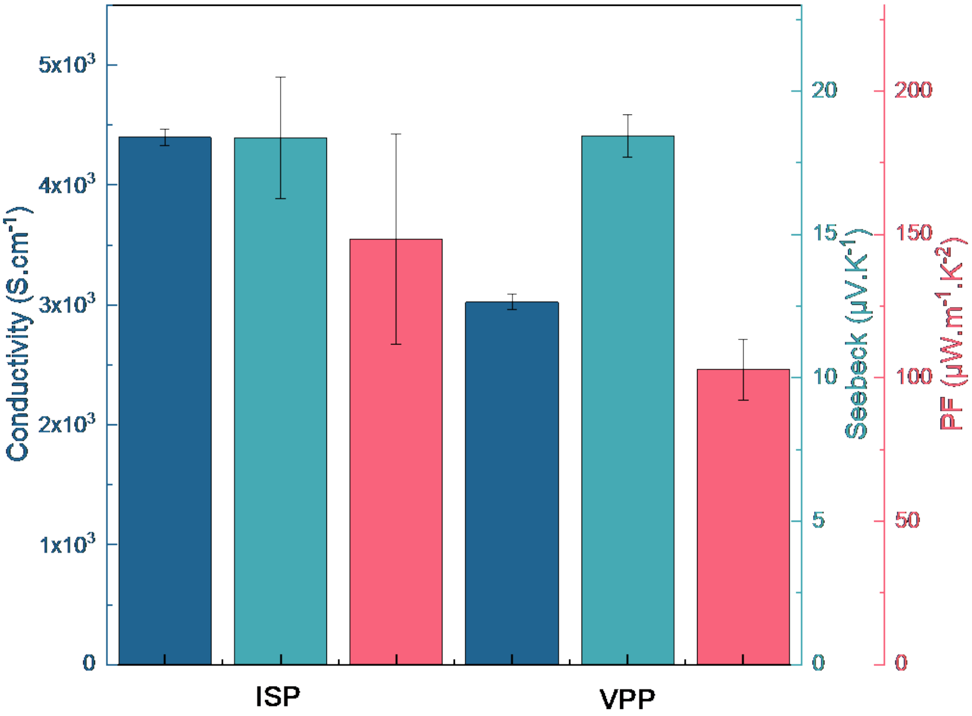

**Figure 5:** Thermoelectric properties of PEDOT:Tos films made by ISP and VPP. Dark blue, cyan and pink bars correspond to the electrical conductivity, Seebeck coefficient and power factor (PF), respectively.

## 4. Conclusion

In-situ chemical polymerization and vapor-phase polymerization are the two main routes to obtain highly conductive PEDOT:Tos thin films. These synthetic processes produce films with the same chemical composition and doping level (22 ± 2 %) which exhibit a semi-metallic behavior. However, at the mesoscopic scale, the two processes lead to different morphological features characterized by a drastically lower roughness for ISP films. Considering paracrystalline disorder, slightly different crystallographic structures are retrieved, and the ISP films present a twice higher relative crystallinity with larger crystallites and a dominating face-on orientation. Such characteristics induce a better charge carrier mobility, responsible for the enhanced conductivity as a similar doping level was evidenced for ISP and VPP films. The Seebeck coefficients are almost equal in both film types which is, within the Mott formula formalism, consistent with same doping level and different charge carrier mobilities. Finally, the enhanced transport properties retrieved for ISP films result in an approximately 34% improvement of the power factor for ISP films.

## Acknowledgments

The authors acknowledge financial support from the Région Aquitaine (Ph.D. grant # 2016-1R10206-00007195). S.P. and F.P. are grateful to the Labex AMADEUS (ANR-10-LABEX-0042-AMADEUS) for financial support. This work was performed within the framework of the Equipex ELORPrintTec (ANR-10-EQPX-28-01) and the Labex AMADEUS (ANR-10-LABEX-0042-AMADEUS) with the help of the French state Initiative d’Excellence IdEx (ANR-10-IDEX-003-02). The authors are grateful to R. LEFEVRE (ELORPrintTec) for the technical support with UPS and XPS measurements.

# References

1 M. N. Gueye, A. Carella, J. Faure-Vincent, R. Demadrille and J. P. Simonato, *Prog. Mater. Sci.*, 2020, **108**, 100616.

2 X. Fan, W. Nie, H. Tsai, N. Wang, H. Huang, Y. Cheng, R. Wen, L. Ma, F. Yan and Y. Xia, *Adv. Sci.*, 2019, **6**, 1900813.

3 O. Bubnova, Z. U. Khan, A. Malti, S. Braun, M. Fahlman, M. Berggren and X. Crispin, *Nat. Mater.*, 2011, **10**, 429–433.

4 I. Petsagkourakis, E. Pavlopoulou, G. Portale, B. A. Kuropatwa, S. Dilhaire, G. Fleury and G. Hadziioannou, *Sci. Rep.*, 2016, **6**, 1–8.

5 A. Zevalkink, D. M. Smiadak, J. L. Blackburn, A. J. Ferguson, M. L. Chabinyc, O. Delaire, J. Wang, K. Kovnir, J. Martin, L. T. Schelhas, T. D. Sparks, S. D. Kang, M. T. Dylla, G. J. Snyder, B. R. Ortiz and E. S. Toberer, *Appl. Phys. Rev.*, 2018, **5**, 021303.

6 M. Cutler and N. F. Mott, *Phys. Rev.*, 1969, **181**, 1336–1340.

7 C. Kittel, *Introduction to Solid State Physics*, John Wiley & Sons, Inc., Hoboken, New Jersey, 2005.

8 N. W. Ashcroft and N. D. Mermin, *Solid state physics*, Harcourt college publishers, Philadelphia, 1976.

9 I. Petsagkourakis, E. Pavlopoulou, E. Cloutet, Y. F. Chen, X. Liu, M. Fahlman, M. Berggren, X. Crispin, S. Dilhaire, G. Fleury and G. Hadziioannou, *Org. Electron. physics, Mater. Appl.*, 2018, **52**, 335–341.

10 G. Kim and K. P. Pipe, *Phys. Rev. B - Condens. Matter Mater. Phys.*, 2012, **86**, 1–5.

11 W. Shi, T. Zhao, J. Xi, D. Wang and Z. Shuai, *J. Am. Chem. Soc.*, 2015, **137**, 12929–12938.

12 R. Brooke, M. Fabretto, N. Vucaj, K. Zuber, E. Switalska, L. Reeks, P. Murphy and D. Evans, *Smart Mater. Struct.*, 2015, **24**, 035016.

13 J.-S. Kim, W. Jang and D. Wang, *Polymers*, 2018, **11**, 21.

14 M. Mueller, M. Fabretto, D. Evans, P. Hojati-Talemi, C. Gruber and P. Murphy, *Polymer*, 2012, **53**, 2146–2151.

15 D. Wu, J. Zhang, W. Dong, H. Chen, X. Huang, B. Sun and L. Chen, *Synth. Met.*, 2013, **176**, 86–91.

16 J. Metsik, K. Saal, M. Uno, R. Lohmus, S. Leinberg, H. Mändar, M. Kodu and M. Timusk, *J. Polym. Sci. Part B Polym. Phys.*, 2014, **52**, 561–571.

17 H. Goktas, X. Wang, A. Ugur and K. K. Gleason, *Macromol. Rapid Commun.*, 2015, **36**, 1283–1289.

18 J. Kim, E. Kim, Y. Won, H. Lee and K. Suh, 2003, **139**, 485–489.

19 T. Park, C. Park, B. Kim, H. Shin and E. Kim, *Energy Environ. Sci.*, 2013, **6**, 788.

20 P. Hojati-Talemi, C. Bächler, M. Fabretto, P. Murphy and D. Evans, *ACS Appl. Mater. Interfaces*, 2013, **5**, 11654–11660.

21 D. Evans, M. Fabretto, M. Mueller, K. Zuber, R. Short and P. Murphy, *J. Mater. Chem.*, 2012, **22**, 14889.

22 C. M. Madl, P. N. Kariuki, J. Gendron, L. F. J. Piper and W. E. Jones, *Synth. Met.*, 2011, **161**, 1159–1165.

23 E. G. Kim and J. L. Brédas, *J. Am. Chem. Soc.*, 2008, **130**, 16880–16889.

24 M. H. Gharahcheshmeh, M. M. Tavakoli, E. F. Gleason, M. T. Robinson, J. Kong and K. K. Gleason, *Sci. Adv.*, 2019, **5**, 1–13.

25 K. E. Aasmundtveit, E. J. Samuelsen, L. A. A. Pettersson, O. Inganäs, T. Johansson and R. Feidenhans'l, *Synth. Met.*, 1999, **101**, 561–564.

26 E. A. Leroy, *X-ray diffraction methods in polymer science*, Wiley-Interscience, Malabar, Florida, 1969.

27 H. Topsoe, *Bulletin*, 1968, **472**, 63.

28 S. Admassie, F. Zhang, A. G. Manoj, M. Svensson, M. R. Andersson and O. Inganäs, *Sol. Energy Mater. Sol. Cells*, 2006, **90**, 133–141.

29 T. Le Truong, N. D. Luong, J. Do Nam, Y. Lee, H. R. Choi, J. C. Koo and H. N. Nguyen, *Macromol. Res.*, 2007, **15**, 465–468.

30 M. Fabretto, C. Jariego-moncunill, J. Autere, A. Michelmore, R. D. Short and P. Murphy, *Polymer*, 2011, **52**, 1725–1730.

31 V. Jain, M. C. Biesinger and M. R. Linford, *Appl. Surf. Sci.*, 2018, **447**, 548–553.

32 G. Zotti, S. Zecchin, G. Schiavon, F. Louwet, L. Groenendaal, X. Crispin, W. Osikowicz, W. Salaneck and M. Fahlman, *Macromolecules*, 2003, **36**, 3337–3344.

33 M. Fabretto, M. Müller, K. Zuber and P. Murphy, *Macromol. Rapid Commun.*, 2009, **30**, 1846–1851.

34 S. G. Im, K. K. Gleason and E. A. Olivetti, *Appl. Phys. Lett.*, 2007, **90**, 88–91.

35 J. Lu, N. J. Pinto and A. G. MacDiarmid, *J. Appl. Phys.*, 2002, **92**, 6033–6038.

36 O. Bubnova, Z. U. Khan, A. Malti, S. Braun, M. Fahlman, M. Berggren and X. Crispin, *Nat. Mater.*, 2011, **10**, 429–433.

37 E. Hosseini, V. Ozhukil Kollath and K. Karan, *J. Mater. Chem. C*, 2020, **8**, 3982–3990.

38 J. Rivnay, S. C. B. Mannsfeld, C. E. Miller, A. Salleo and M. F. Toney, *Chem. Rev.*, 2012, **112**, 5488–5519.

39 J. Dong and G. Portale, *Adv. Mater. Interfaces*, 2020, **7**, 2000641.

40 S. Chen, I. Petsagkourakis, N. Spampinato, C. Kuang, X. Liu, R. Brooke, E. S. H. Kang, M. Fahlman, X. Crispin, E. Pavlopoulou and M. P. Jonsson, *J. Mater. Chem. A*, 2020, **8**, 18726–18734.

41 M. H. Gharahcheshmeh and K. K. Gleason, *Mater. Today Adv.*, 2020, **8**, 100086.

42 X. Wang, X. Zhang, L. Sun, D. Lee, S. Lee, M. Wang, J. Zhao, Y. Shao-Horn, M. Dincă, T. Palacios and K. K. Gleason, *Sci. Adv.*, 2018, **4**, 1–10.

43 J. F. Franco-Gonzalez, N. Rolland and I. V. Zozoulenko, *ACS Appl. Mater. Interfaces*, 2018, **10**, 29115–29126.

44 H. J. Ahonen, J. Lukkari and J. Kankare, *Macromolecules*, 2000, **33**, 6787–6793.

45 E. E. Havinga, C. M. J. Mutsaers and L. W. Jenneskens, *Chem. Mater.*, 1996, **8**, 769–776.

46 W. A. Muñoz, X. Crispin, M. Fahlman and I. V. Zozoulenko, *Macromol. Rapid Commun.*, 2017, **39**, 1700533.

47 A. Sharma, G. Andersson, J. Rivnay, J. F. Alvino, G. F. Metha, M. R. Andersson, K. Zuber and M. Fabretto, *Adv. Mater. Interfaces*, 2018, **5**, 1800594.

48 P. Sehati, S. Braun and M. Fahlman, *Chem. Phys. Lett.*, 2013, **583**, 38–41.

49 S. Duhm, G. Heimel, I. Salzmann, H. Glowatzki, R. L. Johnson, A. Vollmer, J. P. Rabe and N. Koch, *Nat. Mater.*, 2008, **7**, 326–332.

50 O. Bubnova, Z. U. Khan, H. Wang, S. Braun, D. R. Evans, M. Fabretto, P. Hojati-Talemi, D. Dagnelund, J.-B. Arlin, Y. H. Geerts, S. Desbief, D. W. Breiby, J. W. Andreasen, R. Lazzaroni, W. M. Chen, I. Zozoulenko, M. Fahlman, P. J. Murphy, M. Berggren and X. Crispin, *Nat. Mater.*, 2013, **13**, 190–194.